1996ApJ...464..198G

THE ASTROPHYSICAL JOURNAL, 464:198–211, 1996 June 10
© 1996. The American Astronomical Society. All rights reserved. Printed in U.S.A.

# THE SUBARCSECOND RADIO STRUCTURE IN NGC 1068. II. IMPLICATIONS FOR THE CENTRAL ENGINE AND UNIFYING SCHEMES

J. F. GALLIMORE,[1] S. A. BAUM, AND C. P. O'DEA
Space Telescope Science Institute, 3700 San Martin Drive, Baltimore, MD 21218
*Received 1995 June 23; accepted 1995 October 27*

## ABSTRACT

In this paper, we explore the nature of the subarcsecond radio components in the Seyfert nucleus of NGC 1068. The southernmost component (S) is the most likely candidate for the location of the central engine. The integrated spectrum of this component is flat, and the radio brightness temperatures are $T_b \lesssim 3 \times 10^5$ K. The radio emission is probably dominated by thermal emission rather than self-absorbed synchrotron emission. The implication is that the central engine is either intrinsically radio silent or completely obscured at centimeter wavelengths. It seems likely that the thermal emission from the inverted spectrum subcomponent of S (S1) originates near the inner edge of the obscuring torus.

The central component (C) is probably the location of a shock interface between the subarcsecond jet and a dense, molecular cloud. The bending of the radio jet through a projected angle of 20°, the presence of $H_2O$ maser emission, and the local flattening of the radio spectrum lend support for this scenario. We demonstrate that a giant molecular cloud would have the size and mass sufficient to divert the radio jet.

The spectrum of the radio jet steepens very rapidly with distance northward from component S. Characteristic jet spectra are much steeper than those typically found in radio galaxies. Owing to the copious local infrared radiation field, inverse-Compton losses are estimated to be severe and are probably the dominant cause of the observed spectral aging. The Compton loss timescale constrains the velocity of the radio jet to be $v_{\rm jet} \lesssim 5 \times 10^4$ km s$^{-1}$.

There is evidence for Faraday depolarization toward the subarcsecond radio structure. Inner narrow-line region (NLR) clouds alone might cause this depolarization. Unresolved polarization angle gradients and depolarization arising from other internal and external magnetoionic plasmas, such as a hot intercloud medium or a jet cocoon, presumably also contribute to the depolarization.

We also consider the alignment between the radio (MERLIN and Very Large Array) and *Hubble Space Telescope* images. We chose a registration that aligns subcomponent S1 near the symmetry center of the optical/UV polarization and the mid-infrared peak. In this alignment there are striking correspondences between the NLR structure and the radio jet, suggesting that the jet has a strong impact on the NLR.

*Subject headings:* galaxies: individual (NGC 1068) — galaxies: jets — galaxies: nuclei — galaxies: Seyfert — galaxies: structure — radio continuum: galaxies

## 1. INTRODUCTION

The starburst/Seyfert galaxy NGC 1068 displays a broad range of features characteristic of its hybrid nature. At centimeter wavelengths, the nuclear activity is clearly manifested in a kiloparsec scale radio jet. This jet traces down to subarcsecond (tens of parsecs) scales within the nucleus. There it is resolved into a bent triple source (e.g., Gallimore et al. 1996a, hereafter Paper I; Ulvestad, Neff, & Wilson 1987, hereafter UNW). For illustration, the 5 GHz MERLIN image of the sub-arcsecond radio jet is provided in Figure 1 (see also Paper I; Muxlow et al. 1995). Following the convention of Paper I, the compact radio features are labeled components NE, C, and S. Component S is resolved into subcomponents labeled S1 and S2.

Compared to other active galactic nuclei (AGNs) with resolved radio jets, NGC 1068 is relatively close (we adopt $D \approx 22$ Mpc for $H_0 = 50$ km s$^{-1}$ Mpc$^{-1}$, at which the scaling is $1'' \approx 100$ pc). Through aperture synthesis techniques, the radio jet in the nucleus can potentially be resolved down to sub-parsec scales. Such high linear resolution of an active radio nucleus affords the ability to map the radio activity very close to its source, the "central engine." The properties and nature of the sub-arcsecond radio source in NGC 1068 are therefore important to our understanding of the central engine and its interaction with its environs. This understanding may hopefully be applied to more distant Seyfert galaxies and powerful quasi-stellar objects (QSOs) and radio galaxies, insofar as the central engine in NGC 1068 may operate in a manner similar to those powering the more distant analogs.

We have embarked on a detailed study of the radio properties of NGC 1068 to understand better its enigmatic Seyfert nucleus. In Paper I we presented a set of new and archival radio continuum images. We derived from these images basic morphological and continuum spectral properties of the compact and extended features of the subarcsecond radio jet. In this paper (Paper II), we discuss the implications of these results.

We are interested in four particular aspects of the subarcsecond radio jet, presented as follows. First (§ 2), we study the location and nature of the radio emission from the central engine. Second, we consider the nature of the linear radio structure, or jet, connecting the principal radio components (§ 3). Third, we have found evidence for Faraday depolarization toward components NE and S. We consider possible causes for the observed depolarization (§ 4). Fourth, we propose an alignment between the radio

[1] Also Department of Astronomy, University of Maryland, College Park, MD 20742.



© American Astronomical Society • Provided by the NASA Astrophysics Data System

1996ApJ...464..198G



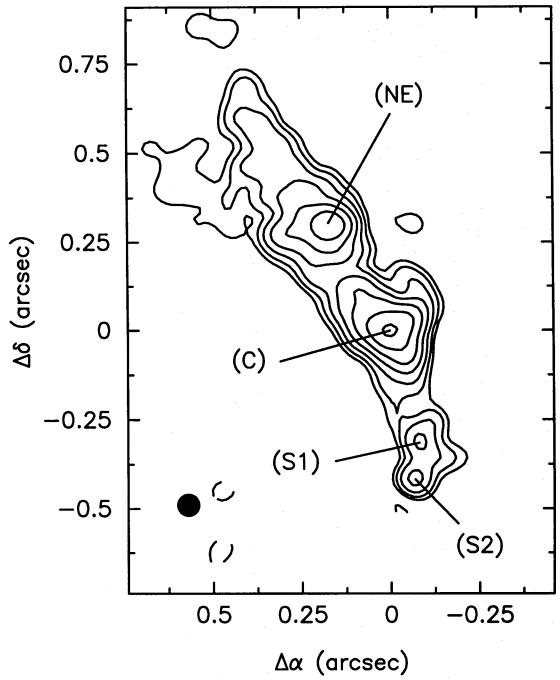


FIG. 1.—Contour map of the 5 GHz MERLIN image. The axes are positional offsets from component C. The contour levels are −0.862, 0.862, 1.73, 3.50, 7.06, 14.23, 28.7, and 57.8 mJy beam$^{-1}$. The beam size, 0.″065 (FWHM), is indicated by the filled circle located to the lower left of the source.

(MERLIN and Very Large Array [VLA]), *Hubble Space Telescope* (*HST*), and mid-infrared images (§ 5). The alignment was chosen to fit a scenario that explains the multiwavelength observations of the near-nucleus environment. We conclude with a summary of our principal results (§ 6).

## 2. THE LOCATION OF THE CENTRAL ENGINE

Gallimore et al. (1996b) found that subcomponent S1 is the most likely candidate for the central engine based on the rotation curve traced by luminous $H_2O$ maser emission surrounding this component. On the other hand, UNW argued for the compact source detected in a European VLBI network (EVN) synthesis image. We consider next the possible nature of the radio emission and the implications for the central engine for both the compact EVN source and component S.

### 2.1. *The Compact EVN Source*

The brightest source on a 1.6 GHz EVN image of NGC 1068 is unresolved at 50 mas resolution (UNW). This compact source is a good candidate for the central engine because its brightness temperature is high, $T_b > 10^8$ K. UNW suggested further that its spectrum may be fairly flat. The EVN observations were not phase referenced, so it is not known with which radio component the EVN source aligns (see the discussion in Muxlow et al. 1995).

At 1.6 GHz the EVN source (86 mJy; Roy et al. 1994, UNW) is brighter than component S (∼40 mJy; Paper I). Therefore, if the EVN source is located at either S1 or S2, it must be variable at 1.6 GHz on a timescale at least as rapid as 10 yr, and the EVN observations must have occurred fortuitously when the source was brighter. (Note that at 22 GHz there is no evidence for variability in any of the radio components; Paper I). Further observations at 1.6 GHz will be required to test the variability of component S.

On the other hand, if the EVN source is associated with either NE or C, its spectrum is not very flat ($\alpha \lesssim -0.4$). The flux densities of components NE and C at 14.5 and 22.5 GHz are each about a factor of 2–3 less than the 1.6 GHz flux (Paper I). The resultant limits to the radio spectral indices are provided in Table 1. These indices are *upper* limits because the MERLIN and VLA observations may be confused with extended, relatively steep-spectrum emission. Since the implied spectrum is about as steep as the surrounding radio jet emission ($-1.1 \lesssim \alpha \lesssim -0.65$; Paper I), we conclude in this case that the EVN source is not a likely site for the central engine. An alternative explanation might be that the compact EVN source marks a compact shock front in the jet flow at component C (§ 3.2, below).

### 2.2. *Component S*

The integrated continuum spectrum of component S is flat ($\alpha \sim -0.1$) from 1.4 to 22 GHz. The spectrum decomposes into contributions from (1) subcomponent S1, whose spectrum is inverted between 5 and 22 GHz ($\alpha = +0.30 \pm 0.06$), (2) subcomponent S2, which has a flat spectrum ($\alpha = -0.15 \pm 0.08$), and (3) a diffuse component whose spectrum is not well determined by our present data but appears to be fairly flat ($\alpha = -0.4 \pm 0.4$; Paper I).

Following the analysis conventionally applied to radio galaxies and QSOs, both subcomponents S1 and S2 are good candidates for a compact, self-absorbed radio core. The torus model offers the possibility that either subcomponent might be free-free absorbed (Neufeld, Maloney, & Conger 1994; Krolik & Lepp 1989). Another possibility is that, like emission from the obscured broad-line region (BLR), we are viewing emission from an obscured flat-spectrum core that has been Thomson-scattered by a reflecting plasma halo into our sight line (as suggested by Antonucci 1993). Given the relatively low brightness temperature of these subcomponents ($T_b \sim 3 \times 10^5$ at 5 GHz; Paper I), another possible explanation is thermal emission. We consider next these possible emission mechanisms in turn.

#### 2.2.1. *Case 1: Synchrotron Emission*

The conventional interpretation of compact, flat- or inverted-spectrum radio emission from the central engines in radio galaxies and QSOs is synchrotron self-absorption (e.g., Blandford 1990; Marscher 1988; Unwin et al. 1985; Cotton et al. 1981). For self-absorption to occur, the brightness temperature must be comparable to the kinetic temperature of the synchrotron electrons. The brightness temperatures of components S1 and S2, however, are in the

TABLE 1

UPPER LIMITS FOR THE SPECTRAL INDEX OF THE COMPACT EVN SOURCE

| | α | |
|---|---|---|
| COMPONENT | 1.6–5 GHz | 1.6–22 GHz |
| NE ..... | $\lesssim -0.6$ | $\lesssim -0.5$ |
| C ..... | $\lesssim -0.4$ | $\lesssim -0.2$ |

NOTE.—Since the registration of the EVN image is uncertain, limits are provided for each of components NE and C.

© American Astronomical Society • Provided by the NASA Astrophysics Data System

1996ApJ...464..198G



range expected for thermal, nonrelativistic electrons. Raising the magnetic field strength permits a lower self-absorption brightness temperature, but for S1 and S2 the magnetic fields would have to be raised implausibly high:

$$B \sim 10^{10}\ \mathrm{G} \times \left(\frac{T_b}{3 \times 10^5\ \mathrm{K}}\right)^{-2}\left(\frac{\nu_c}{5\ \mathrm{GHz}}\right) \quad (1)$$

(Moffet 1975; Slish 1963; Williams 1963), where we have assumed that the optically thin spectral index of the plasma is $\alpha = -0.5$. Of course, there remains the possibility that the intrinsic brightness temperature is much higher but is attenuated by a foreground plasma (case 2). Thus, we rule out otherwise unattenuated, self-absorbed synchrotron emission as the dominant contribution to the spectrum of either subcomponent.

A less conventional interpretation is that the source is optically thin but that the synchrotron electrons have a nearly monoenergetic distribution. This is contrary to the interpretation for radio galaxies and QSOs, in which the jet spectral indices imply a electron energy power-law index $p \sim -2.3$, where the distribution of electron energies is defined by $N(E) \propto E^p$. However, there are flat-spectrum, nonthermal radio "arcs" near the Galactic center that may be synchrotron emission from a monoenergetic distribution of electrons (e.g., Reich et al. 1988; Anantharamaiah et al. 1991). Subcomponents S1 and S2 might be scaled up versions of these arcs. Since the origin of the Galactic radio arcs is not understood, and because the sub-arcsecond radio source in NGC 1068 might be highly depolarized (§ 4), it is difficult to assess this possibility. For comparison, the subcomponents are individually $\sim 120$ times more luminous and about a factor of 15 times smaller in extent than the Galactic radio arcs.

#### 2.2.2. *Case 2: Free-Free Absorbed Compact Source*

Following the suggestion of Antonucci (1993), we consider next the possibility that the spectra of the subcomponents might be explained by free-free absorption of a compact, flat-spectrum source, apropos of the torus models of Neufeld et al. (1994) and Krolik & Lepp (1989). The predicted radio spectrum is inverted, as is the case for subcomponent S1. The spectrum of subcomponent S2, however, is consistent with optically thin free-free emission ($S_\nu \propto \nu^{-0.1}$). Therefore, we consider this option only to explain the inverted spectrum of subcomponent S1.

Based on the two-point spectrum of subcomponent S1, we can estimate the free-free opacity of the plasma along the sight line to the putative flat-spectrum source. Since the detailed structure is unresolved, we consider only a simple model in which a compact, synchrotron self-absorbed source is situated in the middle of a finite, homogeneous slab of thermal plasma (detailed in Appendix A). We take the intrinsic centimeter-wave spectrum in the absence of free-free absorption to have $\alpha = 0$. The limit that emission from the thermal plasma is negligible (i.e., $T_b \lesssim 7000$ K at 5 GHz) gives (1) an upper limit to the compact source flux and (2) a lower limit to the free-free opacity. (The other extreme, in which the radio continuum flux is dominated by thermal emission, is discussed in case [4].) The values are (1) $S_\nu(5\ \mathrm{GHz}) < 18$ mJy and (2) $\tau_{\mathrm{ff}}(5\ \mathrm{GHz}) > 1.1$ (and $\tau_{\mathrm{es}} \ll \tau_{\mathrm{ff}}[5\ \mathrm{GHz}]$, where $\tau_{\mathrm{es}}$ is the Thomson scattering opacity; Appendix A).

For self-absorption to occur at roughly the equipartition field strength ($\sim 1$ mG; Paper I, UNW), the size of the compact source must be smaller than $\theta \sim 0.02$ mas (eq. [1]), much smaller than the measured size of either S1 or S2 ($\theta \sim 40$ mas). Either there must be some contribution from an extended source that is not synchrotron self-absorbed, or the compact emission is seen in reflection.

#### 2.2.3. *Case 3: Reflected Emission from a Compact Source*

Emission from a compact source might be completely obscured due to free-free absorption in the torus (Neufeld et al. 1994; Krolik & Lepp 1989). In this case, components S1 and S2 might be explained by Thomson reflection from the plasma mirror located along the symmetry axis of the torus. The plasma mirror has been resolved by *HST* (Capetti et al. 1995a; Antonucci, Hurt, & Miller 1994). Most of the reflection occurs in a clumpy medium within the inner arcsecond.

There are two predictions made by this scenario. First, due to the wavelength independence of electron scattering, the fraction and orientation of any scattered, unpolarized radio emission from the central engine should agree with the visible/UV polarization properties. Second, the morphology of the scattered radio emission should agree broadly with the polarized visible/UV emission except where the visible/UV emission is attenuated by foreground dust.

These predictions do not appear to hold in NGC 1068. First, the fractional polarization of the radio emission in the inner arcsecond is very low ($f_P \lesssim 3\%$; Paper I) compared to the visible/UV emission ($f_P \sim 16\%$; e.g., Antonucci et al. 1994, Code et al. 1993, Antonucci & Miller 1985). Moreover, the 22 GHz $\boldsymbol{E}$ vector polarization angle is oriented nearly parallel to the radio jet (Paper I), but the intensity weighted optical/UV polarization angle is nearly perpendicular in the radio jet (e.g., Antonucci et al. 1994, and references therein). The morphology also does not agree; the polarized visible/UV emission appears to be correlated with the synchrotron emission from the radio jet (Gallimore, Baum, & Axon 1996c). Component S is instead much smaller than the plasma mirror resolved by *HST* (Capetti et al. 1995a).

That these predictions are invalidated does not preclude the possibility of an obscured radio nucleus. For example, there is evidence for Faraday depolarization toward the inner arcsecond (§ 4 below). Such depolarization might reduce the polarization fraction and rotate the $\boldsymbol{E}$ vectors of any scattered radio emission. Alternatively, scattered, flat-spectrum radio emission may be swamped by synchrotron emission from the jet (Gallimore et al. 1996c). Another possibility is that any hidden radio emission might be intrinsically polarized, thereby reducing the fraction scattered into our sight line.

We cannot specifically rule out this case. Nonetheless, it seems more likely that the emission is thermal in origin because the flat-spectrum emission dims rapidly with distance, i.e., within 10 mas, from component S (Paper I). In contrast, the scattered visible/UV emission peaks some 40 mas from the location of the central engine implied by the symmetry of the visible/UV polarization vectors (Capetti et al. 1995b).

#### 2.2.4. *Case 4: Thermal Emission*

Thermal emission provides the simplest explanation for the two-point spectra of the components S1 and S2 for three reasons. First, it requires the fewest parameters: only characteristic values of $n_e$, $T_e$, and the size of the source. Second, the measured brightness temperatures ($T_b \sim 10^5$ K) are less

© American Astronomical Society • Provided by the NASA Astrophysics Data System

1996ApJ...464..198G

than or comparable to the kinetic temperature inferred for gas exposed to X-radiation from the central engine (e.g., Ueno et al. 1994; Marshall et al. 1993; Krolik & Begelman 1986) or shocked by the radio jet (e.g., Taylor, Dyson, & Axon 1992). Third, the observed sizes of subcomponents S1 and S2 are compatible with estimates of the physical parameters required to produce the observed flux via free-free emission.

We estimated the properties implied by a purely thermal origin for S1 using the simple model described in case 2 and Appendix A. The ranges of permissible free-free and electron scattering opacities are considered more carefully in Appendix B. The resulting constraints are $\tau_{ff}(5\ \mathrm{GHz}) \lesssim 2$ and $\tau_{es} \lesssim 0.1$ to reproduce the observed 5–22 GHz spectral index. In the optically thick limit, $\tau_{ff}(5\ \mathrm{GHz}) \simeq 1.6$ independent of $\tau_{es}$, and in the optically thin limit $\tau_{ff}(5\ \mathrm{GHz}) \approx 10\tau_{es}$.

The physical properties of the thermal plasma can be constrained taking either the optically thick or optically thin limit for the spectral index solutions. First, $T_e \gtrsim T_b$ for either solution, since the plasma may not uniformly cover the beam. Second, $\tau_{ff} \propto n_e^2 l_{\mathrm{cloud}} T_e^{-1.35}$, and $\tau_{es} \propto n_e l_{\mathrm{cloud}}$, where $l_{\mathrm{cloud}}$ is the path length through an individual thermal cloud. Ratios of the limits of $\tau_{ff}$, $\tau_{es}$, and $\tau_{es}^2$ place constraints on $n_e$ and $l_{\mathrm{cloud}}$. These constraints for subcomponent S1 are summarized in Table 2.

The basic constraints for the plasma conditions are $n_e > 10^5\ \mathrm{cm}^{-3}$ and $T_e > 3 \times 10^5$ K. The path length through the thermal plasma, $l_{\mathrm{cloud}} \lesssim 2 \times 10^{-2}$ pc, is much smaller than the measured size of subcomponent S1, which is roughly 4 pc in diameter. A possible explanation is that the thermal plasma is confined to a shell or is composed of many smaller filaments and clumps. The effect of clumping would be to raise the required characteristic values of $T_e$ and $n_e$, reducing the Thomson opacity relative to the free-free opacity for a single cloud. A more sophisticated model is not warranted, however, since the present observations do not constrain the structure within the thermal plasma. Sensitive VLBI observations will be necessary to constrain further the properties of the thermal plasma.

As previously mentioned, the spectrum of subcomponent S2, in contrast with that of S1, is consistent with optically thin thermal emission. $T_e$ is therefore not well constrained by the spectrum. The electron density depends only weakly on $T_e$:

$$n_e \simeq 10^4\ \mathrm{cm}^{-3} \left(\frac{T_e}{10^6\ \mathrm{K}}\right)^{0.35} \left(\frac{l_{\mathrm{cloud}}}{4\ \mathrm{pc}}\right)^{-1/2} . \quad (2)$$

One possible origin for the thermal free-free radio emission is the innermost region of the NLR, where $T_e$ and $n_e$ are expected to be much higher than the average over the entire NLR. This does not seem an unlikely explanation for S2.

TABLE 2

CONSTRAINTS ON PROPERTIES OF THE PUTATIVE THERMAL PLASMA FOR SUBCOMPONENT S1

| Plasma Property | Optically Thick Constraints | Optically Thin Constraints |
|---|---|---|
| $T_e$ ..... | $\gtrsim 3.8 \times 10^5$ K | $\gtrsim 3.1 \times 10^5$ K |
| $n_e$..... | $\gtrsim 4.0 \times 10^6\ \mathrm{cm}^{-3}$ | $\gtrsim 2.5 \times 10^5\ \mathrm{cm}^{-3}$ |
| $l_{\mathrm{cloud}}$..... | $\lesssim 1.2 \times 10^{-3}$ pc | $\lesssim 1.9 \times 10^{-2}$ pc |

NOTE.—Solutions are considered for the optically thick [$\tau_{ff}(5\ \mathrm{GHz}) \simeq 1.6$] and optically thin limits.

However, the gas associated with S1 appears to be very dense, as evidenced by the presence of $H_2O$ masers (Gallimore et al. 1996b) and optically thick free-free radiation. Rather than NLR plasma, a more likely origin for thermal radio emission at S1 is a photodissociation zone (PZ) on the inner face of the molecular torus (e.g., Pier & Voit 1995; Neufeld et al. 1994; Krolik & Lepp 1989). The size of S1 agrees with both (1) the diameter of the maser-emitting region (Gallimore et al. 1996b) and (2) the theoretical predictions of Krolik & Begelman (1986) when scaled to an X-ray luminosity characteristic of Seyfert type 1 nuclei.

The presence of such a dense plasma implies bright nebular emission from inside the torus. Pier & Voit (1995) and Krolik & Kriss (1995) have modeled and discussed the properties of the visible/UV spectrum from the PZ appropriate for the present radio constraints on $T_e$ and $n_e$. Unfortunately, since the PZ is located inside the torus and therefore mostly obscured along our sight line, it will be difficult to test this hypothesis using near-IR/X-ray spectroscopy. Instead, if our interpretation is correct, sensitive VLBI imaging of subcomponent S1 will probably provide the best constraints on conditions inside the torus.

## 3. THE RADIO JET

### 3.1. *The Jet between Components S1 and C*

The continuous spectrum of the sub-arcsecond radio jet steepens with distance from sub-component S1 to C (see Fig. 5 of Paper I). Initially, out to a distance of $\sim 0\farcs1$ (10 pc) from S1, the spectrum is unusually flat, $\alpha \gtrsim -0.2$. As the result of beam averaging, S1 contributes less than 15% of the flux measured $0\farcs1$ away on either of the 5 or 22 GHz images. Confusion with S1 is therefore not the explanation; rather, the extended emission must be dominated by a flat-spectrum component. Following the argument in § 2.2 above, the dominant emission process may be optically thin thermal emission. Another possibility is free-free absorbed, optically thin synchrotron emission. This situation would obtain if, for example, the jet were enveloped by a thermal cocoon close to its origin. Beyond $\sim 10$ pc from S1, the spectrum steepens, and the flux is dominated by synchrotron emission.

### 3.2. *Component C*

Component C is remarkable in that (1) it has a flatter spectrum than the neighboring synchrotron jet emission and (2) at component C the orientation of the radio jet changes from P.A. $\sim 11°$ to P.A. $\sim 33°$ (Paper I). Blue-shifted $H_2O$ maser emission is associated with component C (Gallimore et al. 1996b), as is perhaps the compact VLBI source detected by Roy et al. (1994) and UNW (§ 2.1 above). A conventional interpretation would associate the maser emission with a compact molecular torus or the molecular part of an accretion disk (e.g., Braatz, Wilson, & Henkel 1994; Neufeld et al. 1994) and the compact EVN source with the AGN proper, in analogy with radio galaxies. However, brighter $H_2O$ masers are associated with component S (Gallimore et al. 1996b; Claussen & Lo 1986), and the EVN source does not have a very flat spectrum if it is associated with C (§ 2.1). It is also difficult to imagine that the flat-spectrum plasma responsible for component S, whether the emission is thermal in origin or not, could arise from anywhere but near the central engine.

A similar explanation is that component C results from a shock interaction between the radio jet and a dense molecu-

© American Astronomical Society • Provided by the NASA Astrophysics Data System

1996ApJ...464..198G



lar cloud. To develop this scenario, we consider the supporting evidence: (1) the bend in the radio jet, (2) the radio continuum spectrum, and (3) the presence of $H_2O$ maser emission.

#### 3.2.1. *The Bend in the Jet*

If the radio jet were viewed nearly pole-on, the apparent bend in the jet might be a more modest displacement amplified by projection. This explanation is most convincing in those objects in which there are no lobelike or linear jet structures, so that it appears that we really are looking "down the throat" of the jet. This is not the case for NGC 1068, in which the arcsecond scale structure to the northeast clearly resolves into a jet/lobe structure (Paper I; Wilson & Ulvestad 1983, 1987, 1982; Pedlar et al. 1983). In addition, there is a large-scale outflow or expansion of NLR gas aligned near the radio jet axis in projection (Gallimore et al. 1994; Cecil, Bland, & Tully 1990). Cecil et al. (1990) have modeled the outflow as an expanding conical wind, with the outflow axis oriented along P.A. $\sim 33°$ at an inclination of $i_{\rm cone} \sim 75°$, where $i_{\rm cone} = 0°$ means pole-on. The $H_2O$ maser rotation curve implies a similar inclination for the torus: $i_{\rm torus} \sim 80°$ (Gallimore et al. 1996b). Since the torus/outflow axis probably at least broadly aligns with the axis of the jet, it seems unlikely that at any point the radio jet is viewed very close to pole-on.

A simpler explanation is that the jet is actually diverted in its flow by a pressure gradient in the circumnuclear environment. The jet curves toward the direction of the steepest pressure gradient (e.g., Icke 1991) with a radius of curvature $R_{\rm curv} \approx M^2 s_{\rm grad}$, where $M$ is the jet Mach number and $s_{\rm grad}$ is the scale height of the pressure gradient (e.g., Sparke 1982). As an extreme example of a steep pressure gradient, a shock front would cause a sudden and sharp reorientation or recollimation of the jet flow. Alternatively, the formation of "nozzles" at the shock interface in jet-cloud collisions can accelerate and redirect the jet into more extreme bending angles ($\sim 90°$; Norman & Balsara 1993).

UNW reported that, on their 22 GHz image, the extended emission joining the compact components is gently curved and traces a C-shape. We find no evidence for this curvature on the new, deeper 22 GHz and 5 GHz images (Paper I). The problem may be that the extended emission is very faint at 22 GHz, so the shape of the jet is less certain on the older 22 GHz images. We find that the jet instead follows fairly straight lines joining the adjacent components (Paper I), consistent with a sudden diversion at a shock front.

#### 3.2.2. *The Radio Continuum Spectrum*

The radio continuum spectrum of component C is much brighter and slightly flatter (between 5 and 22 GHz, $\alpha \sim -0.5$) than the spectrum of the surrounding plasma ($-1.1 \lesssim \alpha \lesssim -0.65$). This effect is also seen in the hot spots of more powerful radio sources (e.g., Laing 1989). The implication is that effectively younger, more energetic synchrotron electrons are being introduced at component C, perhaps by way of some reacceleration mechanism. Compression of the jet plasma would give the same general effect.

A possible explanation is first-order Fermi acceleration at a shock front. In the case of a strong, nonrelativistic shock, the expected radio frequency spectral index is $\alpha = -0.5$ (Bell 1978) up to a cutoff frequency dictated by synchrotron losses; downstream the spectrum approaches $\alpha = -1$, assuming continuous injection (e.g., Bregman 1985; Webb, Drury, & Biermann 1984). The spectral behavior of component C and its environs are therefore broadly consistent with Fermi reacceleration at a strong shock. In fact, if the compact EVN source is located at component C, its spectral index is consistent with Fermi reacceleration ($-0.7 \lesssim \alpha \lesssim -0.4$; § 2.1). The compact source might mark the shock front proper. Of course, new VLBI observations will be necessary to orient the location of the EVN source.

Shock compression will also boost the magnetic field strength in the plane of the shock and increase the local synchrotron emissivity, which may explain the brightening at component C. For viewing angles within $\sim 30°$ of the plane of the shock, the polarization of the synchrotron emission should also be enhanced (e.g., Hughes, Aller, & Aller 1985). However, no polarization is detected at component C at either 15 or 22 GHz (Paper I; UNW), and only weak polarization is detected at 5 GHz (Wilson & Ulvestad 1983). If shock compression occurs at component C, it is possible that we are viewing an oblique shock relatively face-on. Another explanation is that the radio emission from component C may have been depolarized by either an internal or intervening thermal medium. Indeed, presented in Paper I and discussed in § 4, we find tentative evidence for such a depolarizing medium.

#### 3.2.3. $H_2O$ *Masers*

Gallimore et al. (1996b) report the discovery of luminous $H_2O$ masers at component C. These masers are blueshifted with respect to the systemic velocity by $\sim 100$ km s$^{-1}$. At the very least, these masers indicate the presence of dense ($n \gtrsim 10^7$ cm$^{-3}$), warm ($T \sim 300$–$400$ K) molecular gas, consistent with the shock picture (see Elitzur, Hollenbach, & McKee 1989). Interstellar $H_2O$ masers are frequently associated with outflow sources in star-forming regions (see Genzel 1986). Following Elitzur et al. (1989), shocks induced in these outflow sources provide a natural heat source in which the (re-)formation of $H_2O$ molecules is enhanced and the maser pump levels are populated through collisions with excited $H_2$ molecules. Continuum emission from the shock front might also power masers in the precursor molecular gas (following the results of Neufeld et al. 1994). The presence of luminous $H_2O$ masers therefore provides circumstantial evidence for shocked molecular gas at component C. Furthermore, there are copious amounts of dense molecular gas within the inner few hundred parsecs (Helfer & Blitz 1995; Tacconi et al. 1994; Jackson et al. 1993) available to interact with the sub-arcsecond jet.

#### 3.2.4. *Properties of the Interacting Cloud*

The size of the interacting cloud should be at least comparable to the width of the jet, $\sim 0\farcs1$ ($\sim 10$ pc), to be able to divert the jet significantly. The intruding cloud should also have been present to divert the jet flow into the northeastern hotspot and lobe; therefore, the cloud must be at least as large as $v_{\rm orb} t_{\rm lobe}$, where $v_{\rm orb}$ is the orbital velocity of the cloud and $t_{\rm lobe}$ is the age of the lobe. We estimate $t_{\rm lobe} \sim 4 \times 10^5$ yr based on the 1.6–15 GHz spectral aging of the northern lobe and adopting an equipartition field strength of $\sim 10^{-4}$ G (Wilson & Ulvestad 1987). The cloud size must therefore be

$$d_{\rm cloud} \gtrsim 40 \text{ pc} \times \left(\frac{v_{\rm orb}}{100 \text{ km s}^{-1}}\right)\left(\frac{t_{\rm lobe}}{3.5 \times 10^5 \text{ yr}}\right) |\cos(\theta)| , \quad (3)$$

© American Astronomical Society • Provided by the NASA Astrophysics Data System

1996ApJ...464..198G



where $\theta$ is the angle between the jet and cloud velocity vectors. For comparison, the emission-line cloud complex sizes resolved in the inner NLR are typically $\gtrsim 0\farcs1$ ($\gtrsim 10$ pc; Macchetto et al. 1994).

The cloud should also be sufficiently massive that it is not accelerated to the jet velocity over the lifetime of the jet/cloud interaction. Following the treatment of Eilek et al. (1984), the cloud mass must be of the order

$$M_{\rm cloud} \gtrsim 400\ M_\odot \left(\frac{r_j}{7.5\ {\rm pc}}\right)^2 \left(\frac{\rho_j}{2\times 10^{-25}\ {\rm g\ cm^{-3}}}\right) \times \left(\frac{v_j}{4000\ {\rm km\ s^{-1}}}\right)\left(\frac{t_{\rm lobe}}{3.5\times 10^5\ {\rm yr}}\right), \quad (4)$$

where we have normalized the jet density ($\rho_j$) and velocity ($v_j$) to the estimates of Wilson & Ulvestad (1987) for their heavier jet model of the northeastern radio lobe. Using their lighter jet model ($v_j \sim 1.5\times 10^4$ km s$^{-1}$, $\rho_j \sim 5\times 10^{-27}$ g cm$^{-3}$), $M_{\rm cloud} \gtrsim 40\ M_\odot$. The jet radius ($r_j$) is based on the jet width measured in Paper I. The mean preshock molecular particle density corresponding to these size and mass estimates is

$$\tilde{n}_{\rm cloud}({\rm H_2}) \sim 0.4\ {\rm cm^{-3}} \left(\frac{M_{\rm cloud}}{200\ M_\odot}\right)\left(\frac{r_{\rm cloud}}{18\ {\rm pc}}\right)^{-3}. \quad (5)$$

For comparison, giant molecular clouds in the disk of the Galaxy have characteristic radii $r_{\rm cloud} \sim 6$–$60$ pc, masses $M_{\rm cloud} \sim 10^3$–$10^6\ M_\odot$, and mean densities $n_{\rm cloud} \sim 20$–$150$ cm$^{-3}$ (e.g., Solomon et al. 1987), all generally meeting or exceeding the requirements for the interacting cloud. $H_2O$ maser emission further signals the presence of dense molecular gas (Gallimore et al. 1996b). Therefore, it seems a very likely explanation that the jet has been diverted at a shock interface with a giant molecular cloud whose orbital path intercepts the jet axis.

### 3.3. *The Jet between Components C and NE*

The jet spectrum steepens from $\alpha \sim -0.5$ at component C to $\alpha \sim -1.5$ at a point midway between C and NE. The 5 GHz surface brightness drops by roughly a factor of 4 over this distance, and the 22 GHz surface brightness drops by roughly a factor of 20 (Paper I). In contrast, the radio surface brightness and spectral index of jets in radio galaxies typically remain fairly constant throughout their lengths. The sub-arcsecond jet in NGC 1068 does not expand appreciably between C and NE. A likely explanation is that the radio synchrotron electrons are experiencing a net energy loss in this region (see Leahy 1991 for a recent review of this topic).

Synchrotron losses are probably too slow to explain the rapid cooling of the radio synchrotron electrons. Inverse Compton losses, however, are expected to dominate synchrotron losses inside the inner arcsecond as a result of the dense infrared radiation field (Braatz et al. 1993; Cameron et al. 1993; Wilson & Ulvestad 1987). Roughly half the integrated, sub-arcsecond scale mid-infrared emission is extended along the radio jet axis. Adopting the Telesco et al. (1984) infrared spectrum (see Wilson & Ulvestad 1987), the photon energy density is roughly $5\times 10^{-7}$ ergs cm$^{-3}$. The ratio of the inverse Compton to synchrotron loss timescales is:

$$\frac{\tau_C}{\tau_S} \sim 0.08 B_{\rm mG}^2 \left(\frac{u_{\rm rad}}{5\times 10^{-7}\ {\rm ergs\ cm^{-3}}}\right)^{-1}, \quad (6)$$

where we have normalized to a characteristic equipartition field strength $B_{\rm mG} = B/1$ mG.

In the absence of effects that would tend to brighten or steepen the spectrum, i.e., local injection or compression, Compton losses would cause the surface brightness to dim exponentially (e.g., Eilek & Hughes 1991). The Compton cooling timescale at 22 GHz therefore constrains the jet velocity:

$$v_{\rm jet} \sim 5\times 10^4\ {\rm km\ s^{-1}} \left(\frac{l/\sin i}{15\ {\rm pc}}\right)\left[\frac{\tau_C(22\ {\rm GHz})}{300\ {\rm yr}}\right]^{-1}, \quad (7)$$

where $l$ is half the projected distance between C and NE, $i$ is the inclination of the jet ($i = 0$ means pole-on), and $\tau_C$ is normalized to its expected value at 22 GHz.

A slower jet is permitted if the emissivity is locally enhanced, i.e., through local injection or compression in the jet plasma. In the case of a homogeneous plasma with uniform local injection, the spectrum would steepen no more than $\Delta\alpha = -0.5$ (Pacholczyk 1970, and references therein), contrary to the observed $\Delta\alpha \sim -1$. Therefore, if local injection or compression occur in this region, conditions in the postshock flow must be inhomogeneous. The sum contributions of newly injected, compressed, and aged plasmas would result in a spectral index change steeper than $-0.5$ and a more gradual decline in surface brightness (Coleman & Bicknell 1988).

### 3.4. *Component NE*

Component NE is similar to component C in two respects. First, the synchrotron spectrum of the jet flattens locally at component NE (Paper I). Second, there is extended emission associated with component NE that is not aligned with the small-scale jet. Local compression or reacceleration of particles in the synchrotron plasma might be the cause. Unlike component C, however, there is no additional evidence for the presence of a shock front. The morphology and spectrum of component NE suggest an interaction with the surrounding interstellar medium (ISM), but this component may be nothing more than a knot in the jet, in analogy with radio galaxy and QSO jets.

## 4. THE NATURE OF THE FARADAY DEPOLARIZING MEDIUM

In Paper I we reported 4–5 $\sigma$ detections of weak ($\sim 3\%$) continuum polarization at 22 GHz toward components NE and S. No polarization is detected in the more sensitive 15 GHz image (Paper I; UNW). Taking the detections at 22 GHz to be real, there is substantial depolarization between 15 and 22 GHz. The cause might be either unresolved polarization angle gradients in the synchrotron plasma or Faraday effects. Unresolved polarization angle gradients are not the only factor, since the synthesis beamwidth at 15 GHz (A-array) observation is smaller than that of the 22 GHz (B-array) observation. Faraday effects must be important if the polarization is real.

The depolarization could be caused by a thermal plasma that is either (1) mixed in with the synchrotron jet material or (2) located in unresolved foreground clouds (e.g., Leahy 1991; Laing 1984). Free-free absorption toward the sub-

© American Astronomical Society • Provided by the NASA Astrophysics Data System

1996ApJ...464..198G



arcsecond radio structure provides independent evidence for an intervening thermal plasma (Pedlar et al. 1983). The extent of the depolarizing medium is roughly 1″ (100 pc), since the northeastern radio structure is not depolarized (Wilson & Ulvestad 1987) and the southwestern radio structure is probably depolarized by ionized gas in the foreground galaxian disk (Gallimore et al. 1994).

Plasma in the inner NLR is a likely candidate for a foreground depolarizing screen. To test this possibility, we consider the magnetic field strength required in individual NLR clouds to produce the observed depolarization. Depolarization would occur because the Faraday depth through individual, unresolved clouds is high, but the Faraday depth is not uniform across the NLR. The mean Faraday rotation angle through individual clouds would have to be at least one radian at 15 GHz to explain the observed depolarization. Assuming that individual NLR clouds are otherwise homogeneous but contain a randomly oriented, tangled magnetic field, the characteristic magnetic field strength is

$$B \gtrsim 5\sqrt{N}\ \mu\mathrm{G}\left(\frac{n_e}{10^3\ \mathrm{cm}^{-3}}\right)^{-1}\left(\frac{l_{\mathrm{cloud}}}{\mathrm{pc}}\right)^{-1}, \qquad (8)$$

where $N$ is the number of magnetic field reversals along the sight line (e.g., O'Dea 1989). We have normalized the electron density and path length to values appropriate for the NLR clouds (e.g., Macchetto et al. 1994; Shields & Oke 1975; Khachikian & Weedman 1971; Osterbrock & Parker 1965).

This lower limit is on the order of the magnetic field strengths typical of the diffuse Galactic ISM (~few $\mu$G; e.g., Kulkarni & Heiles 1987) and less than those of Galactic molecular clouds (up to a few mG; e.g., Roberts et al. 1993, Killeen, Lo, & Crutcher 1992, Crutcher, Troland, & Kozes 1987). The conditions in the NLR clouds are such that, even with very low magnetic field strengths, they can easily cause the observed depolarization.

Presumably the configuration of the depolarizing medium may be more complex and involves contributions from magnetoionic plasmas with widely varying properties and located both within and outside of the radio jet. Examples include thermal plasma entrained in the jet, in a jet cocoon, or in a hot intercloud medium. The present data do not, however, require more sophisticated models for the depolarizing medium.

An implication is that the 1.3 cm continuum emission might also be partially depolarized, so that the intrinsic polarization might be higher. We caution, however, that the present detections of polarization are very weak. It will be necessary to obtain more sensitive observations to confirm the detection at 1.3 cm. Millimeter-wave observations should constrain the level of depolarization at 1.3 cm and might also provide a direct measurement of the Faraday rotation depth toward components NE and S.

## 5. THE ALIGNMENT WITH THE *HST*/FAINT OBJECT CAMERA IMAGES

The circumnuclear region of NGC 1068 has been imaged in visible/UV continuum and line emission with the *HST* [Faint Object Camera (FOC): Macchetto et al. 1994; Planetary Camera (PC): Evans et al. 1991, Lynds et al. 1991]. The visible/UV emission traces an extended, vaguely conical geometry. The popular explanation is that the gas is photoionized by a collimated radiation field originating at the apex of the cone. The orientation of the cone appears to rotate from P.A. = 0° on small scales to P.A. = 30° in the extended NLR gas generally following the behavior of the radio jet (see Wilson & Tsvetanov 1994, and references therein). One possible explanation is that the ionization cone is matter bounded on small scales (compare with NGC 4151, Pedlar et al. 1993; and NGC 3227, Mundell et al. 1995). Alternatively, the apparent bending might be explained by an interaction between the circumnuclear ISM and the expanding radio jet (or a more loosely collimated, but associated, outflow). Line emission would occur near the shock interface between the ISM and radio jet, tracing the bent path of the radio jet (see, e.g., Capetti et al. 1995c; Taylor et al. 1992; Pedlar, Unger, & Dyson 1985). Unfortunately, there is an ~0.″5 registration uncertainty between the *HST* and radio images that precludes an absolute, point-to-point comparison at this time.

Two selective alignments have been presented in the literature. First, Evans et al. (1991) proposed an alignment based on the similar relative spatial orientations of radio components S1, S2, C, and NE and four emission-line clouds they labeled clouds A, B, C, and D (see Fig. 2). Based on the symmetry of the visible/UV polarization vectors, Capetti et al. (1995a) considered placing component S near the high-polarization, "twin-crescent"–shaped continuum structure lying 0.″6 south of cloud B. Capetti et al. (1995b), however, have since revised the location of the central engine based on the post-COSTAR *HST* polarimetry; the new position is somewhat closer to NLR cloud A (Fig. 2).

### 5.1. *Our Preferred Registration*

We consider here an alternative registration, illustrated in Figures 2 and 3, and schematically in Figure 4, that aligns both (1) subcomponent S1 near the position of the peak mid-infrared (12.4 $\mu$m) emission (Braatz et al. 1993) and (2) radio component C with the UV continuum peak located near NLR cloud B. We performed only a translation of the *HST* images to obtain this registration; the relative rotation of the images should be accurate to better than ~2° (Hack et al. 1991). Supporting our registration, Capetti et al. (1995b) have recently and independently located the central engine near our placement of S1 based on new *HST* polarimetry.

The primary motivation for this registration is that it aligns the most likely candidates for the location of the central engine based on independent evidence at different wave bands. Considered below, there are interesting correspondences between the radio jet and NLR structures implied by this alignment. The primary result is that, at least on sub-arcsecond scales, the radio jet and NLR gas may have a strong effect on each other.

### 5.2. *Radio Component C and NLR Cloud B*

There is a good correspondence between the morphology of radio component C and the UV-continuum image of cloud B. At lower surface brightness levels, both regions are vaguely triangular in projection. The eastern and western edges of the triangles are sharp in both cases and align closely in this registration. On the [O III] image, there is a thin line of emission aligned with the radio jet axis. This extended structure originates at cloud B and terminates near a bright UV-continuum feature located between components C and NE. The 5 GHz contours show a similar

© American Astronomical Society • Provided by the NASA Astrophysics Data System

1996ApJ...464..198G



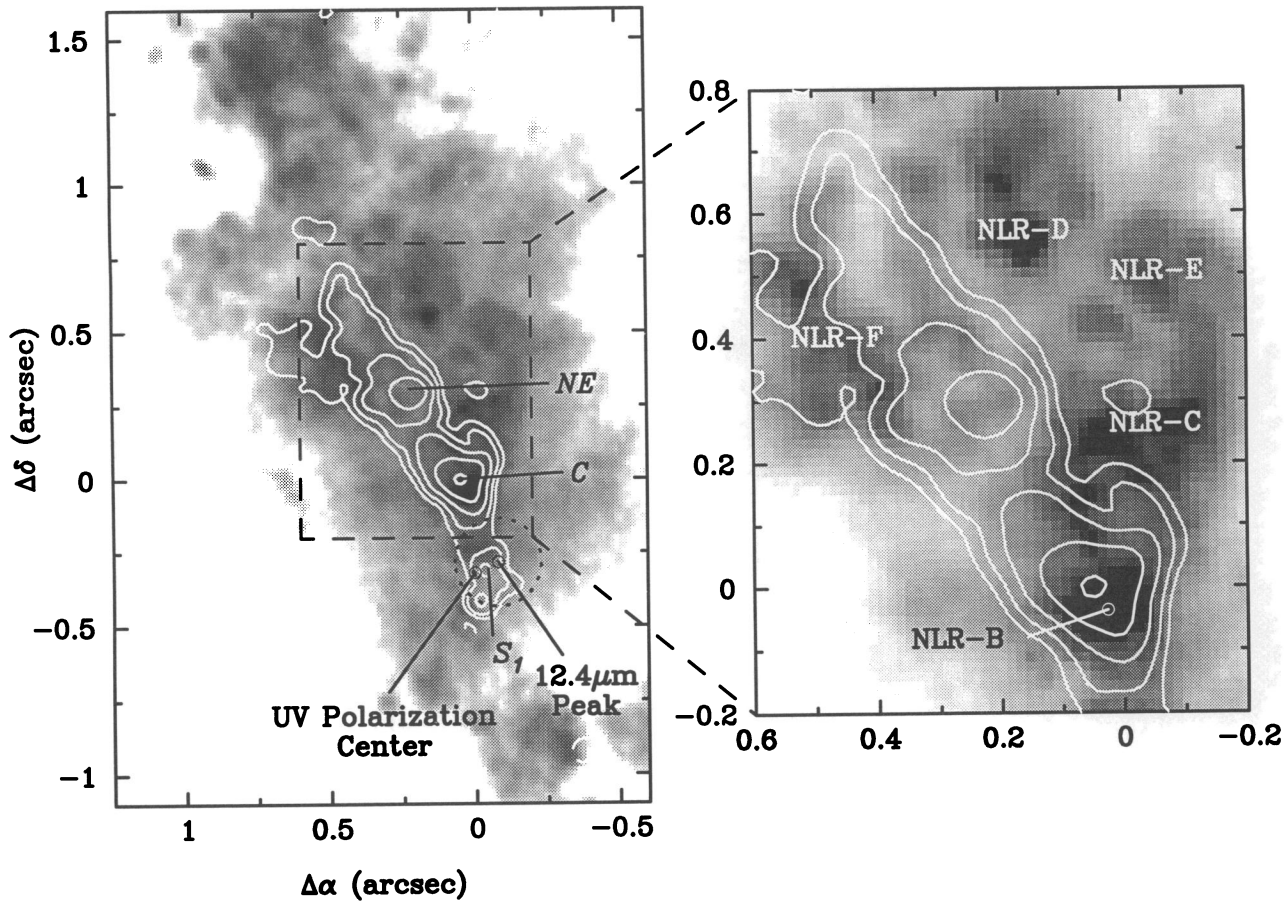


FIG. 2.—*Left*: Overlay of the MERLIN 6 cm image (in contours) on the FOC image of the [O III] λ5007 emission line (gray scale with a logarithmic stretch). The principal radio components NE, C, and S1 are labeled in italics. The position of the 12.4 μm peak, based on the registration of Braatz et al. (1993), is indicated by a dotted circle with a radius corresponding to the registration uncertainty. The position of the symmetry center of the UV polarization *E* vectors is also marked; the formal uncertainty of the position is 0".02–0".06 (Capetti et al. 1996b). *Right*: An enlargement of the region including components NE and C. The FOC image is displayed with a linear stretch to highlight the brightest emission. The locations of the NLR "clouds" A–F are labeled with "NLR-" prefixes. The NLR naming convention is from Evans et al. (1991).

extension away from component C that aligns well with the linear [O III] emission feature. The association suggests further interaction between the jet and the surrounding ISM downstream from the principal shock at component C.

Based on both morphology and kinematics, there is independent evidence for a shock front near NLR cloud B that lends support for our preferred registration. Seen in UV excess (Fig. 3), cloud B resolves into a C-shaped continuum source resembling a bow shock located roughly 5 pc north-northeast (P.A. ~ 20°) of the peak in the [O III] emission (Macchetto et al. 1994). The C-shaped structure is oriented pointing north-northwestward in the downstream direction of the local jet flow in agreement with the jet shock scenario. Macchetto et al. noted that the displacement between the (upstream) emission-line gas and the (shock front) continuum emission are also consistent with that expected in a fast shock with a finite (i.e., not negligible) cooling time (Taylor et al. 1992).

Optical emission-line widths at cloud B are multiply peaked and have broad wings extending to $\pm 2000$ km s$^{-1}$ (Caganoff et al. 1991). In contrast, the local rotation curve peaks at $\pm 400$ km s$^{-1}$ (Gallimore et al. 1996b). It appears that the NLR plasma at cloud B is extremely turbulent. In view of the registration presented here, arguably the simplest explanation is that the jet has accelerated the NLR plasma through shocks.

It will be interesting to compare the emission-line profiles of cloud B with those of the other emission-line clouds to see if cloud B is unique in these characteristics. Follow-up spectroscopy with the *HST*/FOS, or the second-generation STIS instrument, will be necessary to trace the accelerated NLR gas and discriminate it from material in normal galactic rotation. In addition, shock ionization models (e.g., Dopita & Sutherland 1996), in conjunction with COSTAR-corrected *HST* spectroscopy, would provide further tests of this scenario.

### 5.3. *Radio Component NE and NLR Clouds C–F*

Another interesting consequence of this alignment is that there is an anticorrespondence between the [O III] and radio continuum emission in the region surrounding component NE. The NLR cloud complexes C–F lie along the boundary of the sharp surface brightness cutoff on the 5 GHz image. There is, however, very weak radio emission associated with cloud F. Otherwise, it appears as if the radio jet has swept this region clear of emission line gas. There are two possibilities: (1) the jet has truly swept the region clear or (2) the emission-line clouds may have an appreciable free-free opacity so that they suppress any radio emission behind them.

The second possibility can be tested by comparing the surface brightness of [O III] emission from *HST* images

© American Astronomical Society • Provided by the NASA Astrophysics Data System

1996ApJ...464..198G



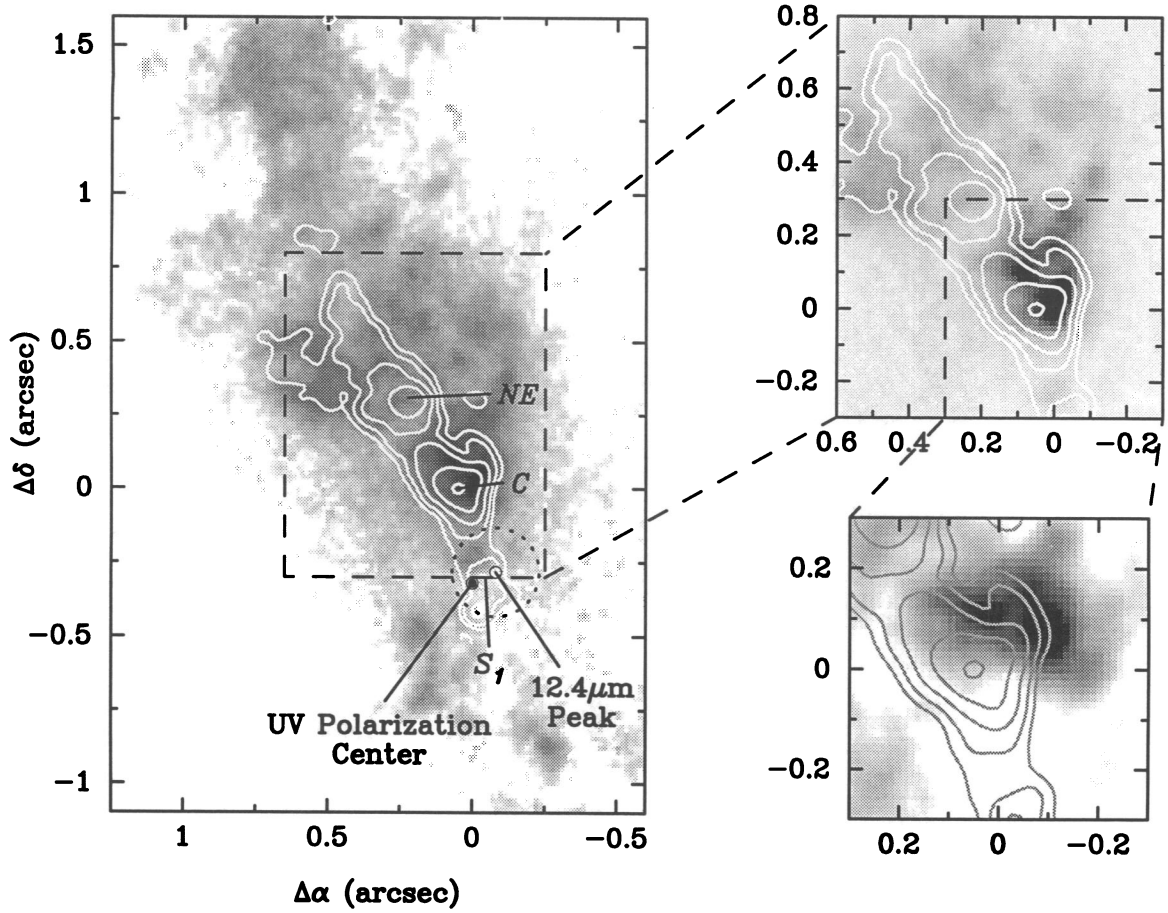


FIG. 3.—Overlays of the MERLIN 6 cm image on the FOC continuum images. *Left*: Overlay of the MERLIN 6 cm image (in contours) on the 2530 Å FOC image (gray scale with a logarithmic stretch). Principal features are marked as in Fig. 2. *Top right*: The same overlay, expanded around components C and NE, but the FOC image is presented with a linear stretch. *Bottom right*: An overlay, expanded around component C, of the MERLIN 6 cm image (contours) over the $\lambda = 2530$ Å/$\lambda = 3720$ Å ratio image (gray scale). Darker gray scale corresponds to a stronger UV excess.

with that predicted by the minimum emission measure (EM in pc cm$^{-6}$) required to absorb out jet emission at 5 GHz. Typical jet surface brightnesses are $\sim$5–10 mJy beam$^{-1}$ on the 5 GHz image. For jet emission to be reduced to below the 3 $\sigma$ level (0.87 mJy beam$^{-1}$) on the 5 GHz image, $\tau_{ff}$(5 GHz) $\sim$ 2 through the NLR clouds. Assuming $T_e \sim 10^4$ K for the emission-line clouds, the inferred emission measure is EM $\sim 2 \times 10^8$ pc cm$^{-6}$. The corresponding H$\alpha$ surface brightness is $S(\mathrm{H}\alpha) = 8.7 \times 10^{-8}$ EM ergs cm$^{-2}$ s$^{-1}$ (Spitzer 1978), or $\sim 4 \times 10^{-10}$ ergs cm$^{-2}$ s$^{-1}$ arcsec$^{-2}$. Empirically, the mean [O III] surface brightness in the NLR is at least a factor of 2 brighter than H$\alpha$ (Adams & Weedman 1975). For comparison, the measured [O III] surface brightnesses over the inner NLR are $\lesssim 5 \times 10^{-12}$ ergs s$^{-1}$ cm$^{-2}$ arcsec$^{-2}$ (Evans et al. 1991). Reconciling this value with that derived from free-free absorption requires $A(\lambda 5007) \gtrsim 2.2$ mag along the sight line to the NLR. This is consistent with the mean extinction to the NLR derived from the Balmer decrement, $A(\lambda 5007) \sim 2.3$ (Adams & Weedman 1975).

Another test is radio emission from the inner NLR clouds. If the NLR clouds are opaque at 5 GHz to absorb out any background radio jet emission, their thermal emission might be detectable at $\nu \leq 5$ GHz. Again taking $T_e = 10^4$ K, the surface brightness at 5 GHz should be $\sim$0.9 mJy $\times$ $C_f$ ($T_e$/10$^4$ K) per 0.″065 beam, where $C_f$ is the covering fraction. This is right at the 3 $\sigma$ detection limit for the MERLIN 5 GHz image. Indeed, 3 $\sigma$ level radio emission is associated with cloud F, but none of the other clouds are detected. However, if the covering fraction is less than unity, or if the temperature in the NLR clouds is less than $10^4$ K, the NLR clouds would not be detected on the MERLIN image.

We conclude that, given the present data, we cannot rule out free-free absorption in the NLR gas as the cause of the anticorrespondence between the radio continuum emission surrounding component NE and the [O III] emission associated with cloud complexes C–F. Still, the anticorrespondence can also be explained by the radio jet having swept the region surrounding component NE free of gas. Again, follow-up spectroscopy with the COSTAR-restored *HST* will be necessary to test these possibilities.

## 6. SUMMARY: A SCENARIO FOR THE SUB-ARCSECOND JET IN NGC 1068

*The radio nucleus.*—The radio continuum emission from subcomponents S1 and S2 is not dominated by a synchrotron self-absorbed component. The central engine must either be intrinsically radio silent or heavily obscured at centimeter wavelengths. The observed radio emission at component S is dominated by either thermal emission from a hot plasma or scattered emission from an obscured compact radio source. If the emission is thermal, the physical properties are broadly comparable to the theoretical predictions for the inner torus (Neufeld et al. 1994; Krolik & Lepp 1989). The bright $H_2O$ masers at component S1

© American Astronomical Society • Provided by the NASA Astrophysics Data System

© American Astronomical Society • Provided by the NASA Astrophysics Data System

1996ApJ...464..198G

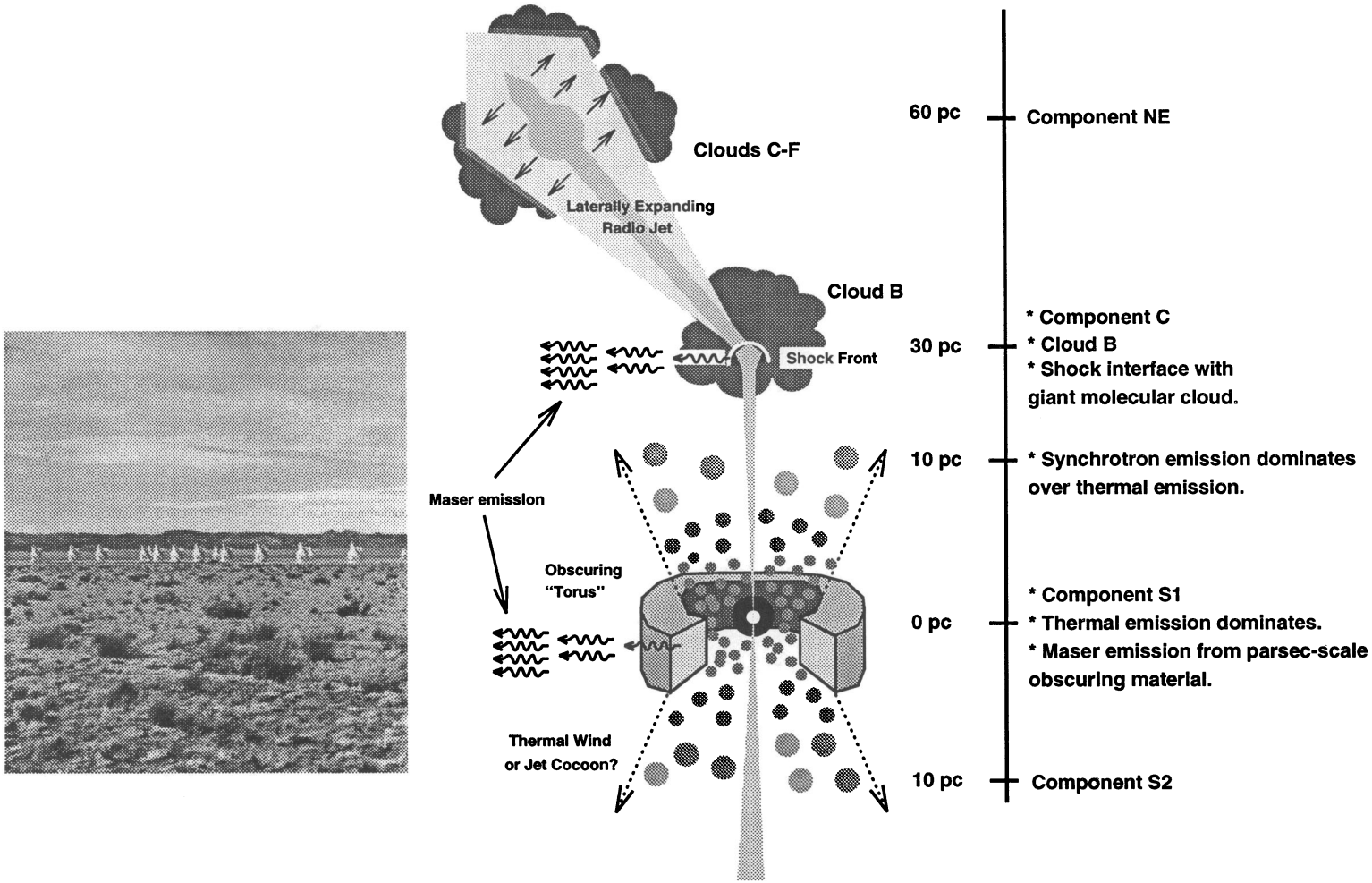


FIG. 4.—A schematic of the sub-arcsecond radio jet in NGC 1068. The schematic is not drawn to a uniform scale. The vertical scale indicates distances along P.A. = 0°.

1996ApJ...464..198G



might arise in a predominantly molecular region outside the free-free emission zone (Gallimore et al. 1996b; Claussen & Lo 1986).

Because of the effects of a foreground, depolarizing medium (§ 4), it is difficult to distinguish any scattered radio waves from this wind. The effects of Faraday depolarization are less severe at millimeter wavelengths, so sensitive millimeter-wave observations may be useful to search for a scattered component to the emission at component S. In any case, based on the radio continuum spectrum alone, component S collectively marks the most probable location for the AGN (see also Muxlow et al. 1995).

*The nature of component C.*—The radio emission at component C appears to arise at a shock interface between the radio jet and a dense molecular cloud. Supporting evidence includes (1) the radio continuum spectrum, which both brightens and flattens locally at component C, (2) the presence of blueshifted $H_2O$ maser emission, (3) the bending of the radio jet at component C, and (4) bright UV emission from the shock front (near cloud B). The implied properties of the interacting cloud are $M_{\rm cloud} \gtrsim 2 \times 10^4\ M_\odot$ and $d_{\rm cloud} \gtrsim 40$ pc. The compact EVN radio source might mark the shock front at which synchrotron electrons are reaccelerated, a possibility that will require new VLBI observations to test.

*The radio jet.*—Emission near the base of the jet is probably dominated by thermal emission from a hot ($\sim 10^5$–$10^6$ K) AGN-driven wind or thermal cocoon enshrouding the radio jet. Beyond $\sim 0\farcs1$ (10 pc) north of subcomponent S1, the flux is dominated by synchrotron emission. Owing to the intense local infrared radiation field, inverse-Compton losses are estimated to be severe. The very steep spectrum of the jet between components C and NE is indicative of nonuniform particle injection through this region. The jet velocity is constrained to be less than about $5 \times 10^4$ km $s^{-1}$.

*The depolarizing medium.*—If the detections of linear polarization at 22 GHz are real, then the nondetection at 15 GHz implies the presence of a depolarizing medium. Clouds in the inner NLR can cause this depolarization if the magnetic field strengths are comparable to those found in the diffuse ISM or giant molecular clouds. The depolarization may presumably include contributions from a thermal plasma entrained in the jet or a hot intercloud medium.

*HST/radio image registration.*—The selective alignment of (1) the mid-infrared peak and subcomponent S1 and (2) radio component C with an apparent shock front ("cloud B") on the *HST*/FOC images produces some provocative correspondences between the radio jet and the inner NLR. There is a linear [O III] emission feature that matches closely the extended radio emission through component C. There are also agreements between the morphologies of cloud B and component C. There is an anticorrespondence between the radio emission near component NE and the inner NLR clouds. Either the jet has swept the region clear of emission-line gas, or the gas is opaque to centimeter-wave radiation.

We wish to thank Alessandro Capetti for providing electronic versions of the *HST*/FOC images. This work benefited from comments from and conversations with Dave Axon, Alessandro Capetti, Reinhard Genzel, Alan Pedlar, Ernie Seaquist, Andrew Wilson, and the participants of the STScI AGN Journal Club. We would also like to thank the referee, Julian Krolik, for suggestions that greatly tightened the arguments presented in the text. The photograph of the VLA was donated by the photographer, Sandra Gallimore. J. F. G. acknowledges support from the STScI Director's Discretionary Fund during part of the course of this work. Further support for this work was provided by NASA through grant number AR-04933.01-92A from the Space Telescope Science Institute, which is operated by the Association of Universities for Research in Astronomy, Inc., under NASA contract NAS 5-26555. This paper represents a portion of J. F. G.'s Ph.D. thesis, submitted in partial fulfillment of the requirements of the Graduate School of the University of Maryland.

## APPENDIX A

## A SIMPLE FREE-FREE ABSORPTION MODEL

In § 2.2 we discuss the possibility that the 5–22 GHz spectrum of subcomponents S1 and S2 are caused either by free-free absorbed synchrotron emission or purely thermal emission. For this discussion, we consider a simple model in which a flat-spectrum synchrotron source is embedded in the middle of a slab of thermal plasma. To estimate the properties of the intervening, thermal plasma, we consider the brightness temperatures implied for the synchrotron and thermal emitting sources as a function of free-free opacity.

For this model, the radiative transfer equation in brightness temperature is

$$T(\nu) = T_0(\nu)e^{-\tau(\nu)/2} + T_e[1 - e^{-\tau(\nu)}]\,, \tag{A1}$$

where $T_0(\nu)$ is the beam-diluted brightness temperature of the synchrotron source at frequency $\nu$, $T_e$ is the beam-diluted electron temperature of the absorbing plasma, and $\tau(\nu)$ is the total optical depth of the thermal plasma. The unknowns in this equation are $\tau(\nu)$, $T_e$, and $T_0(\nu)$. Only measurements at 5 and 22 GHz are available for the subcomponents. Nevertheless, we can constrain $\tau$ for plausible assumptions on the core spectrum. The procedure is to isolate both $T_e$ and $T_0(\nu)$ as functions of $\tau(\nu_1)$, the free-free opacity at one of the two observed frequencies (a subscript "2" will indicate the other frequency). Then we constrain both brightness temperatures to be greater than zero. The physical interpretation is that at the value of $\tau(\nu)$ where $T_0(\nu) \to 0$, the spectrum can be described solely by emission from a thermal plasma. On the other hand, where $T_e \to 0$, emission from the free-free absorbing plasma can be neglected because it is either intrinsically "cold" or very compact.

Assuming that the compact core spectrum is described by a power law of index $\alpha$, the (beam-diluted) electron temperature

© American Astronomical Society • Provided by the NASA Astrophysics Data System

1996ApJ...464..198G



of the intervening plasma as a function of continuum opacity is given by

$$T_e = \frac{T_1/\sqrt{e_1} - T_2/(K_\alpha\sqrt{e_2})}{p_1/\sqrt{e_1} - p_2/(K_\alpha\sqrt{e_2})}, \tag{A2}$$

where $T_1$ and $T_2$ are the measured brightness temperatures at frequencies $\nu_1$ and $\nu_2$, respectively, $e_i \equiv \exp[-\tau(\nu_i)]$, $p_i \equiv 1 - e_i$, and $K_\alpha \equiv (\nu_1/\nu_2)^{\alpha-2}$. The (beam-diluted) brightness temperature of the compact synchrotron source at frequency $\nu_1$ is

$$T_0(\nu_1) = \frac{T_1/p_1 - T_2/p_2}{\sqrt{e_1}/p_1 - \sqrt{e_2}\,K_\alpha/p_2}. \tag{A3}$$

We include a contribution from Thomson scattering to the continuum opacity using the approximate relation $\tau_i \approx \{\tau_{ff}(\nu_i)[\tau_{ff}(\nu_i) + \tau_{es}]\}^{1/2}$ Rybicki & Lightman 1979), where $\tau_{ff}(\nu_i)$ is the free-free opacity and $\tau_{es}$ is the opacity to Thomson scattering, which is independent of frequency. The frequency dependence of the free-free optical depth of a plasma in the radio regime is approximately $\tau_{ff}(\nu_2) = \tau_{ff}(\nu_1)(\nu_2/\nu_1)^{-2.1}$.

Since $\tau_{es}$ is proportional to the electron column density but $\tau_{ff}$ is proportional to the emission measure, it is not possible to isolate a parameter that uniquely sets both opacities without fixing some other parameter (e.g., choosing the electron density as the variable parameter requires fixing the path length through the thermal plasma to determine both $\tau_{es}$ and $\tau_{ff}$). Instead, we chose to examine the brightness temperatures $T_0(\nu_1)$ and $T_e$ as a function of $\tau_{ff}(\nu_1)$ for different fixed values of $\tau_{es}$. In this way we were able to sample the parameter space adequately to estimate the range of brightness temperatures and free-free opacities that might explain the two-point spectrum of subcomponent S1.

Taking $\nu_1 = 4.993$ GHz and $\nu_2 = 22.46$ GHz, we generated plots of $T_0(\nu_1)$ and $T_e$ as a function of $\tau_{ff}(\nu_1)$ for fixed values of $\tau_{es}$. For these calculations, we used the peak surface brightnesses of subcomponent S1 from the 5 and 22 GHz images, both convolved to the same (0.″82) beam size. The results of these calculations are plotted in Figure 5. In Figure 5*a*, for which the Thomson scattering depth is taken to be negligibly small, there are positive solutions for $T_e$ and $T_0(\nu_1)$ only over the narrow range $1.1 \lesssim \tau_{ff}(\nu_1) \lesssim 1.6$. Outside this range either $T_e$ or $T_0(\nu_1)$ must be negative (and therefore unphysical) to explain the observed flux densities. In the limit $T_0(\nu_1) \to 0$, the beam-diluted electron temperature is $T_e = 9.8 \times 10^4$ K. In the limit in which thermal emission is negligible, the beam-diluted source brightness temperature is $T_0(\nu_1) = 1.3 \times 10^5$ K.

In Figure 5*b* we introduce a small but finite Thomson opacity, $\tau_{es} = 0.01$. Because allowing a finite Thomson opacity results in a quadratic dependence between the total continuum opacity and the free-free opacity, there are now two regions of

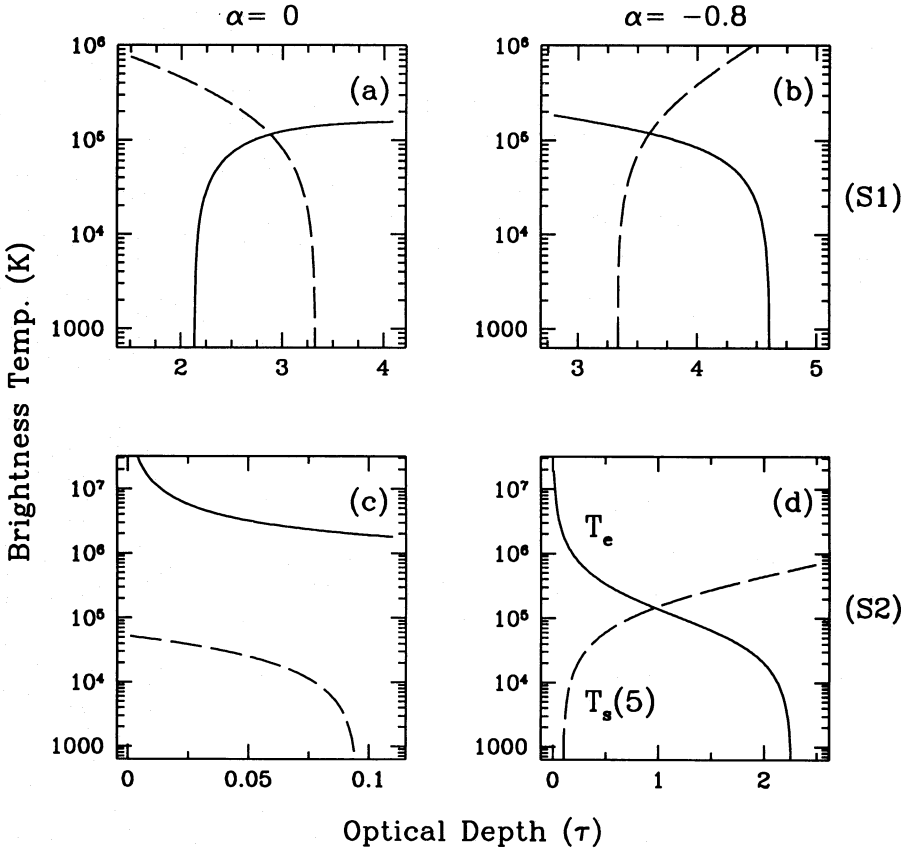


FIG. 5.—Solutions for the free-free absorbing slab model discussed in § 2.2 and Appendix A. The compact synchrotron source is assumed to have a flat continuum spectrum ($\alpha = 0$), and its beam-diluted brightness temperature at 5 GHz is plotted as a solid line. The electron temperature of the thermal plasma is plotted as a dotted line. In (*a*), (*b*), and (*c*) the Thomson opacity is taken to be $\tau_{es} = 0$, 0.01, and 0.1, respectively. Valid solutions for $\tau_{ff}$ occur wherever $T_e$ and $T_0(\nu_1)$ are both nonnegative.

© American Astronomical Society • Provided by the NASA Astrophysics Data System

1996ApJ...464..198G



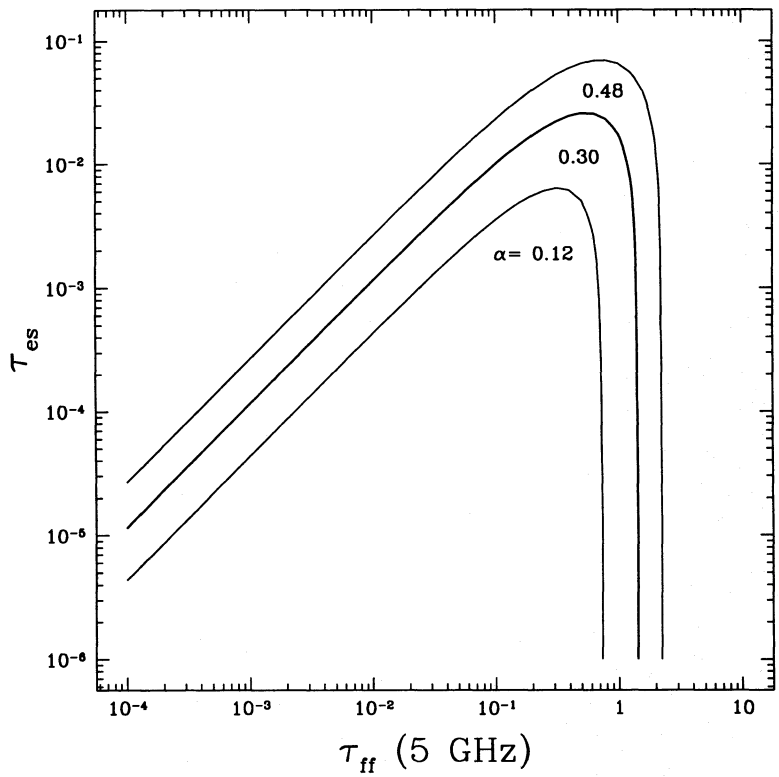


FIG. 6.—Opacity solutions for the purely thermal slab model for subcomponent S1. The curves trace constant values of the 5–22 GHz spectral index measured for subcomponent S1, $\alpha = 0.30 \pm 3\,\sigma$.

acceptable solutions, one optically thick and the other optically thin. The optically thick solution is similar to the solution for Figure 5*a*: $1.1 \lesssim \tau_{\rm ff}(\nu_1) \lesssim 1.4$. At the representative limits the source temperatures are, as in Figure 5*a*, $T_0(\nu_1) = 1.3 \times 10^5$ and $T_e = 9.8 \times 10^4$ K. (This is not surprising, since in the high-opacity solution the adopted Thomson opacity is negible.) The optically thin solution is less restricting, $\tau_{\rm ff}(\nu_1) < 0.08$. In this limit, the beam-diluted electron temperature is $T_e \gtrsim 10^6$ K.

In Figure 5*c*, for which we take $\tau_{\rm es} = 0.1$, there is no longer an optically thick solution that is physical. The "optically thin" solution restricts $\tau_{\rm ff}(\nu_1) < 1.0$. Where $T_e \rightarrow 0$, the beam-diluted brightness temperature of the synchrotron source is $T_0(\nu_1) = 1.2 \times 10^5$ K. Below $\tau_{\rm ff}(\nu_1) \sim 0.5$, the beam-diluted electron temperature is $T_e > 10^5$ K.

In both Figures 5*b* and 5*c*, the denominators of equations (A2) and (A3) go to zero for $\tau_{\rm ff}(\nu_1) = 0.56$ and 2.1, respectively. These asymptotes appear in Figure 5 as vertical lines. However, in the region surrounding and including these asymptotes, the solutions are unphysical and are not considered further.

## APPENDIX B

## A SIMPLE THERMAL FREE-FREE EMISSION MODEL

In § 2.2 we consider the possibility that the inverted radio spectrum of subcomponent S1 might be attributable solely to free-free emission. The measured spectral index constrains the range of electron-scattering and free-free opacities and therefore the properties of the thermal plasma. To estimate the properties of the thermal plasma, we consider, as in Appendix A, above, a simple homogeneous slab model.

The radiative transfer solutions are determined by equation (A1) where, for a purely thermal solution, $T_{0\nu} = 0$. Following the notation of Appendix A, the 5–22.5 GHz spectral index is given by

$$\alpha = 2 + \frac{\log\left[(1 - e^{-\tau_{22.5}})/(1 - e^{-\tau_5})\right]}{\log\,(22.5/5)}\,, \tag{B4}$$

where $\tau(\nu_i) \approx \{\tau_{\rm ff}(\nu_i)[\tau_{\rm ff}(\nu_i) + \tau_{\rm es}]\}^{1/2}$, and $\tau_{\rm ff}(22.5\ {\rm GHz}) = 0.0235 \times \tau_{\rm ff}(5\ {\rm GHz})$.

The solutions for the measured spectral index of sub-component S1, $\alpha = 0.30 \pm 0.18$ (3 $\sigma$ errors), are plotted in Figure 6. The primary constraints derived from these solutions are (1) $\tau_{\rm es} \lesssim 0.1$ and (2) $\tau_{\rm ff}(5\ {\rm GHz}) \lesssim 2$. In the limit in which the plasma is optically thin [$\tau_{\rm ff}(5\ {\rm GHz}) \lesssim 0.5$], solutions are defined by $\tau_{\rm ff}(5\ {\rm GHz}) \approx 10\tau_{\rm es}$. At the other extreme, at which the plasma is optically thick, $\tau_{\rm ff}(5\ {\rm GHz}) \sim 1.6$ independent of the electron-scattering opacity.

© American Astronomical Society • Provided by the NASA Astrophysics Data System

1996ApJ...464..198G



## REFERENCES


Adams, T. F., & Weedman, D. W. 1975, ApJ, 199, 19
Anantharamaiah, K. R., Pedlar, A., Ekers, R. D., & Goss, W. M. 1991, MNRAS, 249, 262
Antonucci, R. 1993, ARA&A, 31, 473
Antonucci, R., Hurt, T., & Miller, J. S. 1994, ApJ, 430, 210
Antonucci, R. R. J., & Miller, J. S. 1994, ApJ, 430, 210
———. 1985, ApJ, 297, 476
Bell, A. R. 1978, MNRAS, 182, 147
Blandford, R. D. 1990, in Active Galactic Nuclei, Saas-Fee Advanced Course No. 20, ed. T. J.-L. Courvoisier & M. Mayor (Berlin: Springer-Verlag), 161
Braatz, J. A., Wilson, A. S., Gezari, D. Y., Varosi, F., & Beichman, C. A. 1993, ApJ, 419, L61
Braatz, J. A., Wilson, A. S., & Henkel, C. 1994, ApJ, 437, L99
Bregman, J. N. 1985, ApJ, 288, 32
Caganoff, S., Kriss, G. A., Antonucci, R. R. J., Ford, H. C., & Hartig, G. 1991, ApJ, 377, L13
Cameron, M., Storey, J. W. V., Rotaciuc, V., Genzel, R., Verstraete, L., Drapatz, S., Siebenmorgen, R., & Lee, T. J. 1993, ApJ, 419, 136
Capetti, A., Axon, D. J., Macchetto, F., Sparks, W. B., & Boksenberg, A. 1995a, ApJ, 446, 155
———. 1995b, ApJ, 452, L87
Capetti, A., Macchetto, F., Axon, D. J., Sparks, W. B., & Boksenberg, A. 1995c, ApJ, 448, 600
Cecil, G., Bland, J., & Tully, R. B. 1990, ApJ, 355, 70
Claussen, M. J., & Lo, K.-Y. 1986, ApJ, 308, 592
Code, A. D., et al. 1993, ApJ, 403, L63
Coleman, C. S., & Bicknell, G. V. 1988, MNRAS, 230, 497
Cotton, W. D., et al. 1981, AJ, 86, 730
Crutcher, R. M., Troland, T. H., & Kazes, I. 1987, A&A, 181, 119
Dopita, M. A., & Sutherland, R. S. 1996, ApJS, 102, 161
Eilek, J. A., Burns, J. O., O'Dea, C. P., & Owen, F. N. 1984, ApJ, 278, 37
Eilek, J. A., & Hughes, P. 1991, in Beams and Jets in Astrophysics, ed. P. Hughes (Cambridge: Cambridge Univ. Press), 100
Elitzur, M., Hollenbach, D. J., & McKee, C. F. 1989, ApJ, 346, 983
Evans, I. N., Ford, H. C., Kinney, A. L., Antonucci, R. R. J., Armus, L., & Caganoff, S. 1991, ApJ, 369, L27
Gallimore, J. F., Baum, S. A., & Axon, D. J. 1996c, in preparation
Gallimore, J. F., Baum, S. A., O'Dea, C. P., Brinks, E., & Pedlar, A. 1994, ApJ, 422, L13
———. 1996b, ApJ, 462, 740
Gallimore, J. F., Baum, S. A., O'Dea, C. P., & Pedlar, A. 1996a, ApJ, 458, 136 (Paper I)
Genzel, R. 1986, in Masers, Molecules, and Mass Outflows in Star Forming Regions, ed. A. Haschick (Westford, MA: Haystack Observatory), 233
Hack, W., Nota, A., Hodge, P., & Jedrzejewski, R. 1991, *HST* Instrument Science Report FOC-052 (Baltimore: STScI)
Helfer, T. T., & Blitz, L. 1995, ApJ, 450, 90
Hughes, P. A., Aller, H. D., & Aller, M. F. 1985, ApJ, 298, 301
Icke, V. 1991, in Beams and Jets in Astrophysics, ed. P. Hughes (Cambridge: Cambridge Univ. Press), 232
Jackson, J. M., Paglione, T. A. D., Ishizuki, S., & Nguyen-Q-Rieu 1993, ApJ, 418, L13
Khachikian, E., & Weedman, D. 1971, Astrofizika, 7, 389
Killeen, N. E. B., Lo, K.-Y., & Crutcher, R. 1992, ApJ, 385, 585
Krolik, J. H., & Begelman, M. C. 1986, ApJ, 308, 55
Krolik, J. H., & Kriss, G. A. 1995, ApJ, 447, 512
Krolik, J. H., & Lepp, S. 1989, ApJ, 347, 179
Kulkarni, S. R., & Heiles, C. 1987, in Galactic and Extragalactic Radio Astronomy, ed. G. L. Verschuur & K. I. Kellermann (Berlin: Springer-Verlag), 95
Laing, R. A. 1989, in Hot Spots in Extragalactic Radio Sources, ed. K. Meisenheimer & H.-J. Roeser (Berlin: Springer-Verlag), 27
———. 1984, in Physics of Energy Transport in Extragalactic Radio Sources, ed. A. H. Bridle & J. A. Eilek (Green Bank: NRAO), 90
Leahy, J. P. 1991, in Beams and Jets in Astrophysics, ed. P. A. Hughes (Cambridge: Cambridge Univ. Press), 100
Lynds, R., et al. 1991, ApJ, 369, L31
Macchetto, F., Capetti, A., Sparks, W. B., Axon, D. J., & Boksenberg, A. 1994, ApJ, 435, L15
Marscher, A. P. 1988, ApJ, 334, 552
Marshall, F. E., et al. 1993, ApJ, 405, 168
Moffet, A. T. 1975, in Galaxies and the Universe, Stars and Stellar Systems, Vol. IX, ed. A. Sandage, M. Sandage, & J. Kristian (Chicago: Univ. Chicago Press), 21
Mundell, C. G., Holloway, A. J., Pedlar, A., Meaburn, J., Kukula, M. J., & Axon, D. J. 1995, MNRAS, 275, 67
Muxlow, T. W. B., Pedlar, A., Holloway, A., Gallimore, J. F., & Antonucci, R. R. J. 1995, MNRAS, submitted
Neufeld, D. A., Maloney, P. R., & Conger, S. 1994, ApJ, 436, L127
Norman, M. L., & Balsara, D. S. 1993, in Jets in Extragalactic Radio Sources, ed. K. Meisenheimer & H.-J. Roeser (Berlin: Springer-Verlag), 229
O'Dea, C. P. 1989, A&A, 210, 35
Osterbrock, D., & Parker, R. 1965, ApJ, 141, 892
Pacholczyk, A. G. 1970, Radio Astrophysics (San Francisco: Freeman)
Pedlar, A., Booler, R. V., Spencer, R. E., & Stewart, O. J. 1983, MNRAS, 202, 647
Pedlar, A., Kukula, M., Longley, D. P. T., Muxlow, T. W. B., Axon, D. J., Baum, S., & O'Dea, C. P. 1993, MNRAS, 238, 863
Pedlar, A., Unger, S. W., & Dyson, J. E. 1985, MNRAS, 214, 463
Pier, E. A., & Voit, G. M. 1995, ApJ, 450, 628
Reich, W., Sofue, Y., Wielebinski, R., & Seiradakis, J. H. 1988, A&A, 191, 303
Roberts, D. A., Crutcher, R. M., Troland, T. H., & Goss, W. M. 1993, ApJ, 412, 675
Roy, A. L., Norris, R. P., Kesteven, M. J., Troup, E. R., & Reynolds, J. E. 1994, ApJ, 432, 496
Rybicki, G. B., & Lightman, A. P. 1979, Radiative Processes in Astrophysics (New York: Wiley)
Shields, G. A., & Oke, J. B. 1975, ApJ, 197, 5
Slish, V. I. 1963, Nature, 199, 682
Solomon, P. M., Rivolo, A. R., Barrett, J., & Yahil, A. 1987, ApJ, 319, 730
Sparke, L. S. 1982, ApJ, 254, 456
Spitzer, L. 1978, Physical Processes in the Interstellar Medium (New York: Wiley)
Tacconi, L. J., Genzel, R., Blietz, M., Cameron, M., Harris, A. I., & Madden, S. 1994, ApJ, 426, L77
Taylor, D., Dyson, J. E., & Axon, D. J. 1992, MNRAS, 255, 351
Telesco, C. M., Becklin, E. E., Wynn-Williams, C. G., & Harper, D. A. 1984, ApJ, 282, 427
Ueno, S., Mushotzky, R. F., Koyama, K., Iwasawa, K., Awaki, H., & Hayashi, I. 1994, PASJ, 46, L71
Ulvestad, J. S., Neff, S. G., & Wilson, A. S. 1987, AJ, 93, 22 (UNW)
Unwin, S. C., et al. 1985, ApJ, 289, 109
Webb, G. M., Drury, L. O., & Biermann, P. 1984, A&A, 137, 185
Williams, P. J. S. 1963, Nature, 200, 56
Wilson, A. S., & Ulvestad, J. S. 1983, ApJ, 275, 8
———. 1987, ApJ, 319, 105
———. 1982, ApJ, 260, 56


© American Astronomical Society • Provided by the NASA Astrophysics Data System